

1
2
3 **A multi-technique approach to determine temporal and spatial variability of groundwater-**
4 **stream water exchange**
5
6

7
8
9 **Running title:** Characterization of groundwater-stream exchange processes
10
11

12
13 **Kasimcan Koruk¹, Koray Kamil Yilmaz^{1*}, Zuhale Akyurek², Andrew Binley³**
14
15

16
17 ¹ Department of Geological Engineering, Middle East Technical University, Ankara, Turkey
18

19 ² Department of Civil Engineering, Middle East Technical University, Ankara, Turkey
20

21 ³ Lancaster Environment Centre, Lancaster University, Lancaster, United Kingdom
22
23

24
25 *Corresponding Author:
26

27 Email: yilmazk@metu.edu.tr
28
29
30
31
32
33

34 Acknowledgements

35
36 This study was funded by TUBITAK (The Scientific and Technological Research Council of Turkey) in the
37 scope of research and development project 115Y041 and fieldworks were performed in cooperation with
38 the General Directorate of State Hydraulic Works, Turkey. The authors would like to thank Çağrı Hasan
39 Karaman, Denis Denizhan Yanmaz, and The General Directorate of State Hydraulic Works personnel for
40 their support and assistance in the fieldworks.
41
42
43
44
45
46
47
48
49
50
51
52
53
54
55
56
57
58
59
60

Abstract

Characterizing the spatio-temporal distribution of groundwater-surface water exchange fluxes is of paramount importance in understanding catchment behavior. A wide range of field-based techniques are available for such characterization. The objective of this study is to quantify the spatio-temporal distribution of the exchange fluxes along the Çakıt stream (Nigde, Turkey) through coupling a set of geophysical techniques and in-stream measurements in a hierarchical manner. First, geological and water quality information were combined at the catchment scale to determine key areas for reach-scale focus. Second, electromagnetic induction (EMI) surveys were conducted along the reach to pinpoint potential groundwater upwelling locations. EMI anomalies guided our focus to a 665 meter-long reach of the stream. Along this selected reach, a fiber-optic distributed temperature sensing (FO-DTS) system was utilized to investigate streambed-temperature profiles at fine spatial and temporal scales. Furthermore, vertical hydraulic gradients and exchange fluxes were investigated using nested piezometers and vertical temperature profiles, respectively, at two potential upwelling locations and a potential downwelling location identified by previous surveys. The results of the study reveal heterogeneity of vertical water-flow components with seasonal variability. The EMI survey was successful in identifying a localized groundwater upwelling location. FO-DTS measurements revealed a warm temperature anomaly during cold air temperature and low streamflow conditions at the same upwelling site. Our point-based methods, namely vertical temperature profiles and vertical hydraulic gradient estimates, however, did not always provide consistent results with each other and with EMI and DTS measurements. This study, therefore, highlights the opportunities and challenges in incorporating multi-scale observations in a hierarchical manner in characterization of the groundwater-surface water exchange processes that are known to be highly heterogeneous in time and space. Overall, a combination of different methods helps to overcome the limitations of each single method and increases confidence in the obtained results.

Key words: Groundwater – Surface water interaction, Electromagnetic Induction, Distributed Temperature Sensing, Streambed Temperature Profile, Hydrogeophysics, Hierarchical Approach, Thermochrons, Exchange Processes

1 Introduction

Surface water and groundwater are interconnected at multiple spatio-temporal scales (Winter et al., 1998). As such, quantification of groundwater – surface water (GW-SW) exchange fluxes is a prerequisite for studies focusing on basin scale water management, water quality and ecological status of water bodies (Sophocleous, 2002; Winter et al., 1998). However, exchange processes often exist with significant heterogeneity in space and time, hence appropriate methods are required that are sensitive to the scale of interest (e.g., Kalbus et al., 2006; Binley et al., 2013; Kennedy et al., 2009; Sophocleous, 2002; Varli and Yilmaz, 2018). Several studies have been performed and new methods and technologies have been adopted to determine GW-SW interaction. Hydraulic head measurements and Darcian flux estimates, differential streamflow discharge measurements, seepage meters, environmental tracers, monitoring of water-quality parameters and geophysical applications are some of widely used methods to determine the GW-SW interaction (e.g., Rosenberry and LaBaugh, 2008; Brodie et al., 2007; Kalbus et al., 2006).

At the point scale, hydraulic head measurements from nested piezometers which are installed at two different streambed depths can be used to calculate vertical hydraulic gradients in the streambed (Conant, 2004). From two or more piezometers installed at the same depth but at different locations, lateral or horizontal hydraulic gradient can be estimated (Kalbus et al., 2006). Temperature is also commonly used as a tracer to determine groundwater-surface water interaction, exploiting the difference between the temperature of groundwater and surface water on daily and seasonal temporal scales (Anderson, 2005). The idea of using temperature as a tracer emerged in the 1960s: the study of Suzuki (1960) focused on predicting water flux through saturated sediments using an analytical solution to the heat flow equation. Studies of Stallman (1963) and Bredehoeft and Papaopulos (1965) followed with modifications to Suzuki's original approach. Lapham (1989) used streambed temperature measurements to quantify vertical groundwater flow. Recently, new analytical and numerical methods have been developed based on the temperature time series records (Hatch et al., 2006; Keery et al., 2007). Hatch et al., (2006) offered 1-dimensional analytical solution to obtain vertical fluid flux from temperature time series obtained from two different depths of streambed. Gordon et al., (2013) employed iButton temperature sensors embedded in steel rods to record vertical temperature profile of the streambed; they obtained vertical water flow velocity from vertical temperature profiles using the VFLUX computer program (Gordon et al., 2012). Although these new methods appear to offer reliable results, they operate at a local scale and thus require many measurements in order to quantify the exchange between groundwater and stream water along a reach (Brodie et al., 2007).

While temperature-based methods, described above, provide temperature measurements at the point scale, Selker et al. (2006a,b) introduced and first applied fiber optic distributed temperature sensing (FO-DTS) technology in the field of hydrology, revealing how measurements can be performed in both time and space.

1
2
3 64 FO-DTS is based on the detection of reactions against temperature anomalies (Raman backscattering) of a
4 65 light source transmitted through a fiber optic cable (Dakin, 1987). Under appropriate surface water-
5 66 groundwater temperature contrast, a fiber-optic cable installed along a streambed can reveal thermal
6 67 anomalies at locations where groundwater upwelling occurs. Many studies have followed the guidance of
7 68 Selker et al. (2006a) and offered calibration techniques and methods to apply FO-DTS (Hausner et al., 2011;
8 69 Krause et al., 2012; Matheswaran et al., 2014; Van de Giesen et al., 2012).

13 70 Geophysical methods have been employed in the field of hydrology at a wide variety of vertical and
14 71 horizontal survey scales (Binley et al., 2015). Crook et al. (2008) illustrates the use of electrical resistivity
15 72 imaging for groundwater-surface water exchange studies: variation in electrical conductivity in the
16 73 streambed may reveal heterogeneity of the streambed architecture, or fluids within them. In relatively small,
17 74 shallow streams such a method is challenging to use because of the need to install electrodes. The
18 75 electromagnetic induction (EMI) technique is a more practical method for detecting local shallow
19 76 heterogeneities beneath surface water bodies in a continuous manner and hence is being increasingly applied
20 77 in the field of hydrology (Binley et al., 2013; Rejiba et al., 2018; Gaona et al., 2019). EMI surveys provide
21 78 an integrated measure of the apparent electrical conductivity over a depth that is a function of the separation
22 79 between transmitter and receiver coils. These measurements allow the estimation of the electrical
23 80 conductivity of the streambed sediments through simultaneous measurement of the surface water's depth
24 81 and conductivity as well as the knowledge of the signal sensitivity function of the sensor (Monsoor et al.,
25 82 2006; Binley et al., 2013). Similar to the electrical resistivity method, EMI can give broad information on
26 83 textural variability of the streambed and also reveal contrasts in pore water ionic composition (Binley et al.,
27 84 2013).

37 85 Whilst each method can be used to quantify certain aspects of the groundwater-surface water interaction
38 86 processes, recent studies have combined various methods at multiple scales to more effectively characterize
39 87 these processes that are known to be highly heterogeneous in space and time (Frederiksen et al., 2018; Varli
40 88 and Yilmaz, 2018; González-Pinzón et al., 2015; Klos et al., 2015; Kalbus et al., 2006). For example,
41 89 Rosenberry et al. (2016) combined physical (seepage meters, wells, piezometers), thermal (FO-DTS,
42 90 infrared, vertical temperature profiles) and geophysical methods (EMI) to characterize the distribution of
43 91 dwarf wedgemussels along upper reaches of the Delaware River. More recently, Gaona et al. (2019)
44 92 revealed how combining FO-DTS and EMI can provide strong insight into groundwater-surface water
45 93 exchange processes along a 50m reach. In this study we reveal how these methods can be combined
46 94 effectively at larger scales.

54 95 The objective of this study is to quantify the spatio-temporal distribution of the exchange fluxes along the
55 96 Çakıt stream (Nigde, Turkey) through coupling a set of geophysical techniques and in-stream measurements

1
2
3 97 in a hierarchical manner. First, a two kilometer-long stream reach with potential groundwater input was
4 98 determined from the results of basin scale major ion chemistry, geological information and
5 99 geomorphological observations. Secondly, geophysical surveys including EMI and FO-DTS surveys were
6 100 conducted at the reach scale to pinpoint potential localized groundwater upwelling sections along the
7 101 streambed. Vertical hydraulic gradients and exchange fluxes were investigated using nested piezometers
8 102 and vertical temperature profiles, respectively, to support the results obtained from the geophysical surveys.

13 14 103 2 Study Area

15
16 104 The study basin covers an area of 529 km² in Nigde province, south of Turkey (Figure 1). The basin is
17 105 characterized by highlands with many steep slopes. The Bolkar Mountains are located to the south of the
18 106 basin reaching up to 3450 m above sea level (a.s.l.) within the basin boundaries. Meteorological data are
19 107 available from a meteorological station located at 1453 m a.s.l., in the west part of the basin that is operated
20 108 by the General Directorate of Meteorology since 1937. Mean monthly air temperature (1937-2017) ranges
21 109 from -1.8 °C (January) to 21.6 °C (July), with measured minimum and maximum air temperature values of
22 110 -21.5 °C (in February) and 37.5 °C (in July). Mean annual precipitation is 343 mm. Mean monthly
23 111 precipitation ranges from 51.2 mm in May to 7.3 mm in August.

24
25
26
27
28
29 112 Çakıt stream is the main stream in the basin and starts from western hills of the basin and discharges to the
30 113 east, where it joins the Alihoca stream. There are three stream gauging stations (SGS) within the basin. The
31 114 upstream gauging station is located on the Darbogaz stream which begins at the confluence point of Kılan
32 115 and Ganimet streams; the other two SGSs are located at the downstream of the basin at Alihoca and Çakıt
33 116 stream branches (Figure 1a). The stream name changes to Darbogaz stream after the Darbogaz SGS and
34 117 joins to upper Çakıt stream. Three SGSs have been in operation since October, 2016. Summer baseflow
35 118 conditions usually occur from July to October within the basin. Average baseflow discharge measured at
36 119 Darbogaz SGS was 0.017 m³/sec in 2018. The upper Çakıt stream is dry during July to October. Average
37 120 baseflow discharge at Alihoca SGS and Çakıt SGS, which are located at the downstream end of the basin,
38 121 are 0.113 m³/sec and 0.180 m³/sec, respectively. Stream discharge at Darbogaz increases at the confluence
39 122 of the Ganimet stream and Kılan stream. The streams are fed by snowmelt during spring. Snowmelt
40 123 originating from southern hillslopes is a strong controlling factor on the high discharge in Darbogaz during
41 124 spring. The average stream channel width of the Çakıt stream is 3.5-4.0 meters, which is controlled by
42 125 topography.

43
44
45
46
47
48 126 Shelf and ophiolites are the predominant geological environments over the basin (Figure 1b). Volcanic
49 127 deposits are the result of volcanism starting from Middle Miocene; they were deposited together with
50 128 terrestrial-alluvial deposits and lacustrine deposits. Geological units exposed over the area are Permian-

1
2
3 129 Jurassic aged Marble and Olistostrome in the south, Upper Cretaceous Ophiolitic Mélange in the form of
4 130 Nappe, Paleocene intercalated clastics-limestone, Eocene limestone, Oligocene clastics, Oligocene,
5 131 Miocene aged Gypsum and evaporites, Eocene-Miocene aged volcanic deposits, and Quaternary-aged
6 132 moraine, travertines, alluvial cones, and alluvium. Gypsum units are exposed over the surface overlaying
7 133 from the west to middle parts of the basin, and they affect the hydrochemical properties of the basin.
8 134 Alluvium units are generally composed of poorly rounded gravel, sand and silt with mud-clay lenses; they
9 135 show unconfined aquifer properties with thicknesses up to 30-40 meters. The main groundwater bearing
10 136 units are alluviums, alluvial cones, travertines and limestone units located in the west of the study area,
11 137 marble and moraine units located in the south of the study area (State Hydraulic Works, 2014).
12
13
14
15
16
17
18 138

19
20 139 **Figure 1 here.**
21
22

23 140 3 Methods

24
25 141 The objective of this study is to quantify the spatio-temporal distribution of the groundwater-stream
26 142 exchange fluxes along the Çakıt stream through coupling a set of geophysical techniques and in-stream
27 143 measurements in a hierarchical manner. First, geological, geomorphological and water quality information
28 144 (Figure 1b) were combined at the catchment scale to determine key areas for reach-scale focus. Major ion
29 145 analyses were conducted at 27 sampling locations in June-2016 to describe the hydrochemical
30 146 characteristics of the surface waters in the basin and their possible relation to geology and exchange fluxes.
31 147 Basin scale analyses were followed by geophysical surveys including EMI and FO-DTS surveys to
32 148 investigate potential groundwater upwelling sections at the reach scale. Furthermore, vertical hydraulic
33 149 gradients and exchange fluxes were investigated using nested piezometers and vertical temperature profiles,
34 150 respectively, at two potential upwelling locations and a potential downwelling location identified by
35 151 previous surveys.
36
37
38
39
40
41
42

43 152 3.1. Electromagnetic Induction Survey

44
45 153 EMI surveys can be used to determine the apparent electrical conductivity of the subsurface. The method is
46 154 based on the generation of a primary electromagnetic field from a transmitter coil, and the measurement of
47 155 a secondary field at a receiver coil, which is affected by the conductivity of the subsurface (McNeil, 1980).
48 156 The depth of investigation is a function of frequency of the induced field and distance between a transmitter
49 157 and a receiver coils (McNeill, 1980). In-stream measurements can be carried out by placing the device above
50 158 the water surface (e.g. in an inflatable vessel). With such a configuration, the apparent electrical
51 159 conductivity is thus a function of the depth of the water column, its electrical conductivity and the bulk
52 160 electrical conductivity of the streambed sediment. Given measurements of stream depth and stream water
53
54
55
56
57
58
59
60

1
2
3 161 electrical conductivity, their effects can be removed from the apparent electrical conductivity (e.g. Binley
4 162 et al., 2013). Variations in electrical conductivity can then be attributed to variations in texture of the river
5 163 bed sediments and/or pore water electrical conductivity (Binley et al., 2013). Under these assumptions, high
6 164 permeability/porosity locations along the streambed inferred by EMI surveys could pinpoint locations of
7 165 potential groundwater upwelling, or contrasts in pore water electrical conductivity can indicate localized
8 166 groundwater sources.

9
10
11
12
13 167 EMI measurements were made with the CMD-1 probe (GF Instruments, Czech Republic), in vertical
14 168 coplanar orientation, giving an effective depth of 1.5 meters. Note that we specifically targeted shallow EMI
15 169 measurements to explore the streambed sediments. The positions of EMI measurements were recorded
16 170 simultaneously using a SATLAB-SLC GPS receiver (Satlab Geosolutions AB, Sweden), and water depth
17 171 was measured with an Onset HOBO U20-001-01 water level data logger which was dragged along the
18 172 streambed. The EC of stream water was measured with EXTECH pH100 pH/conductivity probe.

19 20 21 22 23 173 3.2. Fiber-Optic Distributed Temperature Sensing Technology

24
25 174 A XT-DTS™ (Silixa, United Kingdom) FO-DTS unit was employed for this study, enabling a sampling
26 175 resolution of 25 cm over a measurement range of up to 10 km with a 0.01 °C temperature resolution. A 1-
27 176 km long single steel wall tube armored fiber optic duplex cable (Silixa, United Kingdom) was employed
28 177 together with the XT-DTS™. FO-DTS measurements were performed during June, September and October
29 178 2018 field campaigns. Data were collected for 30 minute periods, each period representing different time
30 179 intervals in a day (see Section 4.3 for details). Measurements were taken at each 0.254 m increment
31 180 continuously for approximately 30 minutes. As each measurement lasted 23 seconds with the XT-DTS™,
32 181 a total of about 80 measurements were made for each 30 minute interval. A double-ended calibration method
33 182 (Van de Giesen et al., 2012) was adopted for the study. Two calibration baths, one hot and one cold, were
34 183 located near the FO-DTS unit. 10-meter long sections of the fiber-optic cable were submerged into
35 184 calibration baths, so that approximately 40 measurements were recorded for each calibration bath
36 185 considering spatial resolution of 0.254 m. Temperatures of the calibration baths were traced using Pt100
37 186 temperature calibration probes (accuracy better than $\pm 0.1^\circ\text{C}$ within temperature range -50°C to $+250^\circ\text{C}$)
38 187 which were provided together with the FO-DTS unit. A battery-powered aquarium pump was used in the
39 188 calibration baths to prevent thermal stratification. Cobbles were laid on cable to maintain the connection
40 189 between streambed and cable at every few meters/where necessary. Burying the cable in the streambed was
41 190 not possible due to presence of pebbles, and cobbles.

3.3. Nested Piezometers and Vertical Hydraulic Gradient Estimation

Piezometers consisting of high density polyethylene (HDPE) pipes having a 32 mm outer diameter and 2.6 mm wall thickness were fabricated with a screen length of 20 cm. Screens were made by cutting slots in the piezometers rather than drilling holes in an effort to have greater connectivity and to minimize clogging. Piezometer bottoms were plugged with plastic pipe caps to prevent vertical flow. For installation of piezometers, a mechanical installation method, similar to that described by Baxter et al. (2003) was followed. The installation unit consisted of a metal pointed inner drive rod and an outer metal tube that prevented collapse of the opening during removal of the drive rod (Figure 2). On the top of these two units, caps were welded to bear hammer blows. Holes on the sides of these caps enabled the use of an iron bar to take the units out of the sediments. Piezometers were installed first by driving the inner drive rod and outer metal tube together into the streambed sediments. The inner drive rod is then removed and HDPE piezometers were inserted in their place. In the final step, the outer metal tube was removed.

Figure 2 here.

Six piezometers were installed within the streambed at 3 different sites, namely P1, P2 and P3 (see Section 4.4 for locations). Two of the piezometer sites coincide with locations of high apparent electrical conductivity anomalies (from EMI) in the upstream section; the third site is situated at the downstream end of the study site with low to intermediate EMI measured electrical conductivity values. The piezometers at each site were nested, consisting of one shallow and one deep piezometer. The shallow piezometers were installed at depths that ranged between 36 cm and 43 cm, whereas the deep piezometers were installed at depths that ranged between 85 cm and 102 cm. Note that many studies that measure vertical hydraulic gradients in streams do not use nested piezometers – typically head from only one piezometer is compared with the surface-water stage to determine a vertical hydraulic gradient. However, having nested piezometers at each location helps to check the consistency of the results.

Piezometers P1, P2 and P3 were installed on 27-June, 28-June and 18-September-2018, respectively. Shallow and deep piezometers are denoted by “S” and “D”, respectively (for example, P1-D denotes deep piezometer at site 1). Water levels were measured manually in piezometers P1 and P2 between 28-June and 7-November-2018, and in piezometers P3 between 19-September and 7-November-2018 using a Solinst® Model 107 TLC meter (Solinst Canada Ltd., Georgetown, Ont., Canada). Piezometers were purged prior to manual water level measurements to ensure hydraulic connection (no clogging) and measurements were made after water levels were stabilized. Surface water stage was also measured manually at the piezometer sites. Water level fluctuations in piezometers P2 and P3 were monitored continuously with a 10-minute logging interval for the period 27-October-2018 to 7-November-2018 using HOBO® U20-001-01 pressure

223 loggers (Onset Corporation, USA). A pressure transducer was deployed on the streambed at site P2 to
224 continuously monitor the surface water stage during this time period.

225 Hydraulic head measurements from nested piezometers and surface water stage were used to calculate
226 vertical hydraulic gradient (VHG) values, and hence the direction of streambed vertical flux at the point
227 scale. Negative VHG values indicate upwelling flux direction while positive values indicate a downwelling
228 flux direction.

229 3.4. Vertical Flux Determination from Vertical Temperature Profiles

230 Vertical water flux through the streambed were estimated from diurnal variations in streambed vertical
231 temperature profiles. 1-Wire iButton Temperature loggers (Maxim Integrated® DS1922L) having 0.0625
232 °C resolution, 0.5 °C accuracy at -10°C to 65°C temperature range were used. iButtons were water-proofed
233 with PLASTI DIP® rubber coating and embedded on wooden dowels at two different configurations (Figure
234 3). Initially a configuration with two iButtons (Figure 3a) was used at sites P1 and P2 in June 2018. However,
235 due to failure of one iButton at site P2, flux calculation was not possible for this site in June. To avoid such
236 a failure in further campaigns, we optionally included a 3-iButton configuration where deemed necessary.
237 iButtons were shielded with metal washers to ensure proper thermal conductivity with the streambed. They
238 were set to record the temperature every 10 minutes to make sure that the diurnal temperature variation was
239 properly captured. iButton temperature profiles were recorded in three different sites (P1, P2 and P3) with
240 time periods ranging from 5 to 16 days.

241 **Figure 3 here.**

242 Vertical water fluxes were estimated using VFLUX program – a vertical fluid heat transport solver (Gordon
243 et al., 2012) based on the Hatch et al. (2006) amplitude method. Typical values of sediment and water
244 thermal properties suggested by the program developers were used; thermal dispersivity (0.001 m), thermal
245 conductivity (0.0045 cal/(s·cm·°C)), volumetric heat capacity of the water (1.0 cal/(cm³·°C)), volumetric
246 heat capacity of the sediments (0.5 cal/(cm³·°C)) and total porosity (0.28).

247 4. Results

248 4.1. Determination of the Location of the Reach-Scale Study Area

249 Major ion analysis performed at the basin scale is illustrated in a Piper diagram (Figure 4) and fluid electrical
250 conductivity (EC) values at the sampling locations are provided on the geology map (Figure 1b). Note that
251 the samples are arranged according to river branches from upstream towards downstream (Figure 1a).

1
2
3 252 **Figure 4 here.**
4

5 253 The upper Çakıt stream branch has the highest total dissolved solids, specifically attributed to the gypsum
6 units ($\text{CaSO}_4 \cdot 2\text{H}_2\text{O}$) dissolving high concentrations of sulfate and calcium. In contrast, the Alihoca stream
7 254 branch shows the lowest total dissolved solids with higher concentrations of bicarbonate and calcium
8 255 compared to other ions measured along this branch. Similar to the Alihoca branch, the Ganimet and
9 256 Darboğaz stream branches are also characterized by low total dissolved solids. The upper Çakıt stream
10 257 branch becomes slightly diluted towards downstream due to tributaries draining volcanic deposits to the
11 258 north. The upper Çakıt stream branch and Darboğaz branches merge immediately downstream of sampling
12 259 locations 4 and 11 (Figure 1), respectively, to form the Çakıt stream, reflecting mixed ion concentrations.
13 260 Along the Çakıt stream, sulfate and carbonate concentration increase from sampling location 13 to 14 due
14 261 to a confluence with a tributary draining gypsum unit. The confluence with a northerly tributary before
15 262 sampling location 15 further increases ion concentrations, specifically sodium, sulfate and chloride.
16 263 According to the Piper diagram shown in Figure 4, the hydrochemical facies of upper Çakıt and downstream
17 264 parts of Çakıt are calcium-sulfate type, whereas the Ganimet, Darboğaz, Kılan and upstream part of the
18 265 Çakıt stream branches are calcium-bicarbonate type waters. Low total dissolved solids concentrations in the
19 266 Alihoca, Ganimet and Darboğaz stream branches together with steep stream gradients were interpreted as
20 267 the sign of less groundwater influx potential. The discharge in the upper Çakıt is significantly low and the
21 268 stream is not accessible due to steep valley sides and relatively steep streambed slopes. Moreover, the
22 269 downstream part of the Çakıt is also characterized by steep valley sides and relatively steep streambed
23 270 slopes.
24 271

25
26 272 Considering the results of the major ion analysis, high amount of alluvium deposits, gentle streambed slopes,
27 273 accessibility and the information obtained from local water users (indicating groundwater contribution to
28 274 the stream along the reach) a 2-km reach in the upstream part of the Çakıt stream, situated between sampling
29 275 locations 12 and 14, was selected as the study reach (Figure 1) where groundwater-surface water exchange
30 276 processes was to be further investigated. Individual manual discharge measurements at the study reach on
31 277 2-July-2018 and 11-July-2018 were done in order to understand the water balance of the study reach. On 2-
32 278 July-2018 discharge observed at Darbogaz SGS was $0.210 \text{ m}^3/\text{sec}$. At this time, the upper Çakıt stream was
33 279 dry, and discharge at P2 and P1 (installed piezometers explained in section 3.3) was $0.358 \text{ m}^3/\text{sec}$ and 0.378
34 280 m^3/sec . On 11-July-2018 discharge observed at Darbogaz SGS was $0.103 \text{ m}^3/\text{sec}$, the upper Çakıt stream
35 281 was dry, and discharge at P2 and P1 was $0.325 \text{ m}^3/\text{sec}$ and $0.301 \text{ m}^3/\text{sec}$, respectively.

36 282 4.2. Electromagnetic Induction Survey

37 283 The first EMI survey was performed along the 2-km reach identified in Section 4.1 on 31-January-2018
38 284 (Figure 5). Note that the entire reach shown in Figure 5 is equivalent to the reach indicated in red in Figure
39
40
41
42
43
44
45
46
47
48
49
50
51
52
53
54
55
56
57
58
59
60

1
2
3 285 1a, and the stream reach within the rectangle in Figure 5 is equivalent to the study reach shown in Figure
4 286 6a. A major conductive anomaly was detected during this reconnaissance survey. To further investigate this
5 287 anomaly location together with locations without anomalies in an affordable manner, a 665 m reach was
6 288 selected as the study area for investigation of groundwater and surface water interaction processes in a more
7 289 detailed manner using other methods (Figure 6). A second EMI survey was conducted on 27-June-2018
8 290 along this more focused study area. The depth of stream water ranged from 0 to 80 cm (mean value of 29.3
9 291 cm) along the reach during the EMI survey; the electrical conductivity of the stream water was 894 $\mu\text{S}/\text{cm}$.
10 292 EMI surveys were repeated in September and October-2018 and revealed the same anomaly pattern
11 293 observed in June- 2018. Note that a barrier was constructed by local residents at the middle of stream reach
12 294 to divert the water for irrigational purposes. Such a barrier may have an effect on the hydrological
13 295 characteristic of the reach, as discussed later.

14 296 **Figure 5 here.**

15 297 **Figure 6 here.**

16 298 4.3. Fiber-Optic Distributed Temperature Sensing

17 299 Table 1 lists the DTS measurement periods, minimum, mean and maximum values of the measured top-of-
18 300 streambed temperatures, together with air temperature data collected from the nearest meteorological
19 301 station, and daily stream discharge values collected from the Çakıt stream gauging station. It can be seen
20 302 that there is a marked difference in air temperature on measurement period of October compared to June
21 303 and September measurement periods. Moreover, stream discharge is also relatively lower in October than
22 304 the values in June and September.

23 305 **Table 1 here.**

24 306 Figure 7 shows the FO-DTS measurements taken on 18-September-2018 13:28-13:53 and on 26-October-
25 307 2018 07:31-08:02. Focusing on Figure 7b it can be seen that the top-of-the-streambed temperature values
26 308 increases with time (x-axis) indicating warming of stream water in response to increasing air temperature
27 309 (Figure 7a). More importantly, however, temperature values along the transect (y-axis) are highly variable
28 310 with a marked decrease at the pooled upstream part of the barrier due possibly to increase in stage, and a
29 311 marked increase at the downstream of the barrier (325-328m; the location of the barrier is shown in Figure
30 312 6) due possibly to the surface heating of the pooled water behind the barrier. High variability in temperature
31 313 along the transect (Figure 7b and 7c) is possibly due to the marked solar radiation and vegetation shading
32 314 effects. With groundwater temperature values at around 14°C (based on piezometer measurements), possible
33 315 groundwater inflow from the streambed would be indicated by sustained cold temperatures along the x-axis.
34 316 However, FO-DTS measurements did not indicate any variation in the temperature along the streambed that

1
2
3 317 could be attributed to groundwater inflow in the June and September 2018 field campaigns. Shading effects,
4 318 stream water temperature values being close to the groundwater temperature values and high discharge
5 319 conditions (turbulence) result in unfavorable conditions for the detection of groundwater inflow using FO-
6 320 DTS measurements (Table 1). Moreover, in the presence of relatively coarse-grained streambed sediments,
7 321 the fiber optic cable could not be buried into the streambed. This situation presented another unfavorable
8 322 condition that is known to result in difficulty in detecting thermal anomalies unless groundwater inflow is
9 323 significant (Tristram et al. 2015; Lowry et al. 2007).

10
11 324 FO-DTS measurements on 26-October-2018 (Figure 7d-f) were taken early in the morning (7:31am-
12 325 8:00am) under cold (3 °C air temperature) and cloudy weather conditions hence resulting in minimal shading
13 326 effect and marked differences in stream water and groundwater temperatures. Moreover, stream discharge
14 327 was also lower compared to the observed values in September field campaign. Locations with groundwater
15 328 inflows would be indicated by sustained warmer temperatures along the x-axis in Figure 7e, and warm
16 329 anomalies in mean temperatures (Figure 7f). This situation is observed at a distance of around 550m along
17 330 the transect, close to piezometers P2 and P3 indicating groundwater inflow at this location detected by the
18 331 FO-DTS measurements. Figure 7f also shows that the stream water temperature decreases consistently in
19 332 the downstream direction. This may indicate that streamflow that gets warmer by the influx of relatively
20 333 warm groundwater through the streambed at the upstream of the study area, cools down slightly downstream
21 334 where stream water recharges groundwater.

22
23
24
25
26
27
28
29
30
31
32
33 **Figure 7 here.**

34
35 336 Figure 8 shows the mean temperature of the FO-DTS measurements taken on 26-October-2018 07:31-08:02
36 337 (Figure 8b) and 12:32-13:02 (Figure 8c), and the corresponding EC data inferred from the EMI survey
37 338 conducted in June 2018. It can be seen from Figure 8 that both EMI measured EC values and mean
38 339 temperature values from the FO-DTS measurements show an anomaly at around 550 meters, hence
39 340 consistently indicating upwelling groundwater at this location. The mean values of temperature
40 341 measurements taken on 26-October-2018 at 07:31-08:02, 10:51-11:21 and 12:32-13:02 successfully
41 342 indicated this warming anomaly at the top-of-the-streambed 550 meters upstream of the DTS unit. Note
42 343 that, the effect of solar radiation and shading increased gradually from the measurement period 07:31-08:02
43 344 (Figure 8b) towards 12:32-13:02 (Figure 8c) with the rising sun and resulted in high variations in the
44 345 temperature profile. Thus, solar radiation/shading effects should be avoided as much as possible to more
45 346 clearly identify groundwater signals in FO-DTS measurements.

46
47
48
49
50
51
52
53 347 **Figure 8 here.**

4.4. Nested Piezometers and Vertical Hydraulic Gradient Estimation

Figure 9 shows the vertical hydraulic gradient values (VHG) calculated by manual water level measurements in piezometers and surface water at sites P1, P2 and P3 (see Figure 6 for locations). Site P1 shows consistent positive VHG values indicating strong downward flux that is increasing in magnitude from June to November 2018. Site P2 is characterized by consistent upward gradient until 20-September-2018, and later shows slight upward and downward gradient based on measurement combinations. Note that the magnitude of the VHG is substantially lower compared to that at site P1. After 20-September-2018 the response of the water level after purging at P2-D was very low which could be due to clogging of P2-D, hence the results of VHG calculations involving P2-D were deemed as suspicious after this date (these values are marked with circles in Figure 9b). At Site P3, VHG values calculated from individual and nested piezometers were negative (-1.6% to -8%) indicating upward flux on 20-September-2018 and gradually changed to slightly positive values after 24-October-2018 (for example +0.2% to +4.3% on 24-October 2018) indicating no or minor downward flux after this date. Note that retrieval of correct head gradient data is challenging for piezometers placed directly in the streambed (Anibas et al., 2011). This situation is more notable in the presence of small hydraulic gradients, such as at sites P2 and P3, which increases the sensitivity of the results to measurement errors.

Figure 9 here.

To observe the vertical hydraulic gradients at piezometer sites in a continuous manner, HOBO® pressure transducers were installed at selected piezometers and surface water for the period 27-October to 7-November-2018. A total of five pressure transducers were deployed: –near site P1 for atmospheric correction, P2-S, P2 surface water, P3-S and P3-D. P2-D was neglected due to clogging. The VHG at site P3 was calculated using piezometers P3-D and P3-S, and at site P2 using the surface water level data together with piezometer P2-S (Figure 10). The VHG values at site P3 vary between -0.2% (upward flux) and +1.6% (downward flux) with a more or less diurnal cycle, but the dominant character at this site is slight downward flux for this period (Figure 10a). At site P2 minor upward flux was evident with VHG values varying narrowly around -0.5% with a diurnal signal (Figure 10b). Note that a diurnal signal in water level measurements could be due to thermal artifacts in total pressure transducer readings (McLaughlin and Cohen, 2011).

Figure 10 here.

The results of VHG have shown that while downstream of the study site (P1) was characterized by strong downward gradient, the upstream part of the study area, namely P2 and P3 sites, was characterized by lower

379 hydraulic gradient magnitudes changing from upwelling towards neutral to slightly downwelling starting
380 from late October, 2018 indicating seasonal variation in the direction of the gradient.

381 4.5. Vertical Flux Determination from Vertical Temperature Profiles

382 Vertical flux values were estimated from diurnal temperature variations at two different depths using the
383 amplitude method of Hatch et al., (2006). For example, Figure 11a-11d shows the air temperature during
384 the October-November 2018 measurement period, together with the raw temperature data series, amplitude
385 inference, and vertical flux estimation results at site P3. Diurnal variations in temperature measurements
386 lower than sensor precision were deemed unreliable. However, it is also important to note that low diurnal
387 variations can be the sign of strong upwelling. Table 2 summarizes the vertical flux estimates for three
388 measurement periods. Since Site P1 is characterized by strong downward VHG from piezometers,
389 temperature-based vertical flux was only estimated in June-July 2018 and indicates downward fluid flux
390 ranging between $(+2.2 \times 10^{-6}) - (+2.5 \times 10^{-6})$ m/s. While inferred flux behavior at P2 is in an upward direction
391 in September-October 2018 with values ranging between $(-5 \times 10^{-7}) - (-2 \times 10^{-6})$ m/s, this changes to a
392 downward direction with values ranging between $(+6 \times 10^{-7}) - (+1 \times 10^{-6})$ m/s at a depth of 9.5 cm for the 28-
393 October-2018 to 02-November-2018 period (Table 2). Site P3 is characterized by consistent upward flux
394 direction in both September-October 2018 and October-November 2018 periods with vertical flux values
395 ranging between $(-1 \times 10^{-6}) - (-2 \times 10^{-5})$ m/s and $(-2 \times 10^{-6}) - (-3 \times 10^{-6})$ m/s, respectively.

396 Note that these vertical flux values were estimated using the typical values of sediment and water thermal
397 properties suggested by the VFLUX program developers (see Section 3.4). The sensitivity toolbox of the
398 VFLUX program was used to investigate the possible errors in modeled vertical flux due to these assumed
399 thermal properties. The results of the one-at-a-time sensitivity analysis indicated that the modeled vertical
400 flux values are most sensitive to the sediment thermal conductivity parameter. For example, when the
401 sediment thermal conductivity value was decreased by 50%, the modeled vertical flux range between $(-4.2 \times 10^{-6}) - (-5.6 \times 10^{-6})$ m/s (nearly two-fold increase in magnitude) and when the thermal conductivity value
402 was increased by 50%, the modeled vertical flux range between $(+3.5 \times 10^{-7}) - (-3.2 \times 10^{-7})$ m/s (nearly ten-
403 fold decrease in magnitude with change in flux direction for a certain period) at site P3 for the October-
404 November 2018 period. Note that the assumed sediment thermal conductivity value utilized in this study
405 represents an average value between the limits of measured streambed sediment thermal conductivity values
406 reported in the literature (Sebok and Muller, 2019).

408 **Figure 11 here.**

409 **Table 2 here.**

5. Discussion of the Results

The objective of this study was to quantify the spatio-temporal distribution of the groundwater-stream exchange fluxes along the Çakıt stream in a hierarchical manner. The hierarchical approach started at the basin scale and focused on stream reach scale in a step-wise manner using geology, geomorphology, major ion analyses, electromagnetic induction surveys, fiber-optic distributed temperature sensing technology, nested piezometers and streambed vertical temperature profiles.

The study has shown that EMI survey is an efficient and effective method to identify zones within streambed sediments which may indicate localized upwelling locations. The EMI survey was conducted using the GF Instruments CMD-1 probe, which is only capable of taking measurements at single depth. However, performing EMI surveys at multiple depths would provide a stronger conceptualization of the streambed sediments (Binley et al., 2013; Rejiba et al., 2018) and possibly underlying hydrogeological architecture (Rosenberry et al., 2016). Although EMI surveys were performed in September and October, 2018, the results were not reliable due to the distorted coordinates of the data. Under cloudy and rainy weather conditions, GPS devices (even with high sensitivity) can fail to give exact position in highly vegetated areas, and therefore weather conditions need to be considered for the techniques that requires highly sensitive coordinate data. In this study an EMI survey was conducted along a 2-km reach of the Çakıt stream, which is considerably longer compared to previous studies focusing on EMI surveys to locate exchange flux location; for example, Binley et al. (2013) and Gaona et al. (2019) utilized EMI survey along a 200 m and a 45 m reach, respectively. Although dense vegetation along the stream and changing river bed conditions presented difficulties in EMI surveys, the results provided spatial patterns of stream bed conductivity that in turn helped to successfully infer the local subsurface flow paths as highlighted by Robinson et al. (2008). Interpretation of the EMI measurements relies on a significant contrast in upwelling pore water electrical conductivity and more diffusive groundwater upwelling will not be detected.

The application of FO-DTS provided promising results under certain conditions including cold weather (marked temperature difference between stream water and groundwater); minimal shading effect (early morning and cloudy conditions) and low streamflow conditions (less turbulent mixing along the streambed) (Matheswaran et al., 2014). An important finding of this study is that, under favorable conditions listed above, the FO-DTS temperature anomaly location coincided with the location of the EMI EC anomaly. This result indicates that these two independent methods supported each other and hence they may complement each other at different scales. While EMI survey could be conducted readily over long distances as long as the stream conditions permit, FO-DTS measurements could be utilized at focused reaches to support EMI survey results. Observation of transient conditions such as seasonal variation and flood events would also provide useful information on temporal variability in the exchange fluxes (Gaona et al., 2019).

1
2
3 443 The vertical flux values estimated from iButton thermochrone temperature sensors and vertical hydraulic
4 444 gradient values obtained from nested piezometers provided quantitative insight for the stream reach at the
5 445 point-scale (Constantz, 2008; Kalbus et al., 2006). Both vertical temperature profiles and vertical hydraulic
6 446 gradients agreed with the EMI and DTS surveys and indicated upward vertical water flow direction in
7 447 upstream locations P2 and P3 during 18-September-2018 to 3-October-2018 period. However, these point-
8 448 based methods did not always provide consistent results with each other and with EMI and DTS
9 449 measurements during the 26-October-2018 to 7-November-2018 measurement period. This result could be
10 450 explained by the fact that point-scale methods, being highly sensitive to local conditions, may not be
11 451 indicative of the heterogeneity of the exchange processes at the broader scale that could be revealed by the
12 452 EMI and FO-DTS data that are integrated over a range of scales. This heterogeneity of exchange processes
13 453 in time and space highlights the importance incorporating multi-scale observations in a hierarchical manner
14 454 in characterization of the groundwater-surface water exchange processes. Overall, a combination of
15 455 different methods helps to overcome the limitations of each single method and increases confidence in the
16 456 obtained results.

17 457 In summary, incorporation of the geophysical methods, namely EMI and DTS, enabled identification of
18 458 potential groundwater upwelling locations along the streambed, which would not have been possible with
19 459 point-based methods alone due to the large extent of the study area. The hierarchical approach presented in
20 460 this study could easily be transferred to other locations provided that the necessary instruments are available
21 461 for measurements at various scales. Our recommendations for future applications include performing EMI
22 462 surveys sensitized to multiple depths to infer both hydrogeological structure and streambed heterogeneity,
23 463 and utilizing solar panels for energy source to enable continuous monitoring of the temperature profile along
24 464 the reach with the FO-DTS instrument. Moreover, increasing the point-based data collection locations could
25 465 provide further insight into local heterogeneity, however this option would come with a cost in terms of
26 466 time and budget (Conant, 2004) which were not available for this study and hence recommended for future
27 467 studies.

28 468 6. Conclusion

29 469 In summary, the results indicate that the studied stream reach show different characteristics at downstream
30 470 and upstream locations. While downwelling is the dominant behavior for the downstream of the study reach,
31 471 upwelling is evident at some locations of the upstream of the study reach during the early part of the study
32 472 period.

33 473 The study has shown that EMI surveys which can be conducted at long stream reaches in a relatively short
34 474 time period could be utilized as a valuable reconnaissance method to locate preferential groundwater-stream

1
2
3 475 exchange locations. Moreover, FO-DTS can be further utilized as a complimentary method over shorter
4 476 distances to provide continuous observations in time and space in support of EMI surveys. In this study, a
5 477 high EC anomaly location obtained from the EMI survey coincided with the location of a temperature
6 478 anomaly observed by FO-DTS. The joint use of these methods is a significant highlight of the study. Point-
7 479 based methods of vertical hydraulic gradient estimation from hydraulic head measurements and vertical flux
8 480 estimation from vertical temperature transects can provide quantitative results to support EMI and FO-DTS
9 481 measurements once anomaly locations are determined with EMI and FO-DTS surveys. Our results indicate
10 482 that point-based methods may not always agree with the EMI and DTS surveys, due to mismatch between
11 483 the representative scales and highly heterogeneous nature of the streambed exchange processes. However,
12 484 the use of different set of techniques that are sensitive to different space and time scales in a hierarchical
13 485 manner helps to overcome the limitations of each single method and increases confidence in the obtained
14 486 results.
15
16
17
18
19
20
21
22
23
24
25
26
27
28
29
30
31
32
33
34
35
36
37
38
39
40
41
42
43
44
45
46
47
48
49
50
51
52
53
54
55
56
57
58
59
60

1
2
3
4 502 **References**
5

- 6 503 Anderson, M. P. (2005). Heat as a ground water tracer. *Ground Water*, 43, no. 6: 951-968,
7
8 504 doi.org/10.1111/j.1745-6584.2005.00052.x.
- 9
10 505 Anibas C, Verbeiren B, Buis K, Chormański J, De Doncker L, Okruszko T, Meire P, Batelaan O (2012) A
11
12 506 hierarchical approach on groundwater-surface water interaction in wetlands along the upper
13 507 Biebrza River, Poland. *Hydrol. Earth. Syst. Sci.*, 16:2329–2346. doi:[10.5194/hess-16-2329-2012](https://doi.org/10.5194/hess-16-2329-2012)
- 14
15 508 Baxter, C., Hauer, F. R., and Woessner, W. W. (2003). Measuring groundwater–stream water exchange:
16
17 509 new techniques for installing minipiezometers and estimating hydraulic conductivity.
18
19 510 *Transactions of the American Fisheries Society*, 493-502.
- 20
21 511 Binley, A., Hubbard, S. S., Huisman, J. A., Revil, A., Robinson, D. A., Singha, K., and Slater, L. D.
22
23 512 (2015). The emergence of hydrogeophysics for improved understanding of subsurface processes
24 513 over multiple scales. *Water Resour. Res.*, 51 , 3837–3866, doi:10.1002/2015WR017016.
- 25
26 514 Binley, A., S. Ullah, A. L. Heathwaite, C. Heppell, P. Byrne, K. Lansdown, M. Trimmer, and H. Zhang
27
28 515 (2013), Revealing the spatial variability of water fluxes at the groundwater-surface water
29 516 interface. *Water Resour. Res.*, 49, 3978-3992, doi:10.1002/wrcr.20214.
- 30
31 517 Bredehoeft, J. D., and Papaopulos, I. S. (1965). Rates of vertical groundwater movement estimated from
32 518 the Earth's thermal profile. *Water Resour. Res.*, 1, 325-328,
33
34 519 <https://doi.org/10.1029/WR001i002p00325>.
- 35
36 520 Brodie, R., Sundaram, B., Tottenham, R., Hostetler, S., and Ransley, T. (2007). *An Overview of Tools for*
37
38 521 *Assessing Groundwater-Surface Water Connectivity*. Canberra: Bureau of Rural Sciences.
- 39
40 522 Conant, J. B. (2004). Delineating and quantifying ground water discharge zones using streambed
41
42 523 temperatures. *Ground Water*, 243-257.
- 43
44 524 Constantz, J. (2008). Heat as a tracer to determine streambed water exchanges. *Water Resour. Res.*, 44,
45
46 525 W00D10, doi:10.1029/2008WR006996.
- 47
48 526 Crook, N., Binley, A., Knight, R., Robinson, D. A., Zarnetske, J., and Haggerty, R. (2008). Electrical
49
50 527 resistivity imaging of the architecture of substream sediments. *Water Resour. Res.*, 44, W00D13,
51
52 528 doi:10.1029/2008WR006968.
- 53
54
55
56
57
58
59
60

- 1
2
3 529 Frederiksen R.R., Christensen S., and Rasmussen K.R. (2018). Estimating groundwater discharge to a
4 530 lowland alluvial stream using methods at point-, reach-, and catchment-scale. *Journal of*
5 531 *Hydrology*, 564: 836-845.
- 6
7
8 532 Gaona, J., Meinikmann, K., and Lewandowski, J. (2019). Identification of groundwater exfiltration,
9 533 interflow discharge, and hyporheic exchange flows by fibre optic distributed temperature sensing
10 534 supported by electromagnetic induction geophysics. *Hydrological Processes*, 33:1390–1402.
11 535 <https://doi.org/10.1002/hyp.13408>.
- 12
13
14
15 536 González-Pinzón R, Ward AS, Hatch CE, Wlostowski AN, Singha K, Gooseff MN, Haggerty R, Harvey
16 537 JW, Cirpka OA, and Brock JT. 2015. A field comparison of multiple techniques to quantify
17 538 groundwater–surface-water interactions. *Freshwater Science* 34: 139-160.
- 18
19
20
21 539 Gordon, R. P., Lautz, L. K., and Daniluk, T. L. (2013). Spatial patterns of hyporheic exchange and
22 540 biogeochemical cycling around cross-vane restoration structures : Implications for stream
23 541 restoration design. *Water Resour. Res.*, 49, 2040–2055, doi:10.1002/wrcr.20185.
- 24
25
26 542 Gordon, R. P., Lautz, L. K., Briggs, M. A., and McKenzie, J. M. (2012). Automated calculation of vertical
27 543 pore-water flux from field temperature time series using the VFLUX method and computer
28 544 program. *Journal of Hydrology*, 142-158.
- 29
30
31 545 Hatch, C. E., Fisher, A. T., Revenaugh, J. S., Constantz, J., and Ruehl, C. (2006). Quantifying surface
32 546 water–groundwater interactions using time series analysis of streambed thermal records: method
33 547 development. *Water Resour. Res.*, 42, W10410, doi:10.1029/2005WR004787.
- 34
35
36
37 548 Hausner, M. B., Suarez, F., Glander, K. E., and Van de Giesen, N. (2011). Calibrating Single-Ended
38 549 Fiber-Optic Raman Spectra Distributed Temperature Sensing Data. *Sensors*, 11, 10859-10879;
39 550 doi:10.3390/s111110859.
- 40
41
42 551 Kalbus, E., Reinstorf, F., and Schirmer, M. (2006). Measuring methods for groundwater, surface water and
43 552 their interactions: a review. *Hydrol. Earth Syst. Sci.*, 10, 873-887, doi.org/10.5194/hess-10-873-
44 553 2006.
- 45
46
47
48 554 Keery, J., Binley, A., Crook, N., and Smith, J. W. (2007). Temporal and Spatial Variability of
49 555 groundwater - surface water fluxes: Development and application of an analytical method using
50 556 temperature time series. *Journal of Hydrology*, 336, 1-16, doi:10.1016/j.jhydrol.2006.12.003.
- 51
52
53
54
55
56
57
58
59
60

- 1
2
3 557 Kennedy, C. D., Genereux, D. P., Corbett, R., and Mitasova, H. (2009). Spatial and temporal dynamics of
4 558 coupled groundwater and nitrogen fluxes through a streambed in an agricultural watershed. *Water*
5 559 *Resources Res*, 45, W09401, doi:10.1029/2008WR007397.
6
7
8
9 560 Klos, P.Z., Rosenberry, D.O., Nelson, G.R. (2015) Influence of hyporheic exchange, substrate
10 561 distribution, and other physically linked hydrogeomorphic characteristics on abundance of
11 562 freshwater mussels. *Ecohydrology* 8: 1284-1291.
12
13 563 Krause, S., Blume, T., and Cassidy, N. J. (2012). Investigating patterns and controls of groundwater up-
14 564 welling in a lowland river by combining Fibre-optic Distributed Temperature Sensing with
15 565 observations of vertical hydraulic gradients. *Hydrol. Earth Syst. Sci.*, 16, 1775–1792,
16 566 doi:10.5194/hess-16-1775-2012.
17
18
19 567 Lapham, W. W. (1989). Use of Temperature Profiles Beneath Streams to Determine Rates of Vertical
20 568 Ground-Water Flow and Vertical Hydraulic Conductivity. Denver: U.S. Geological Survey
21 569 Water-Supply Paper 2337.
22
23
24
25 570 Lowry, C.S., Walker, J.F., Hunt, R.J., and Anderson, M.P. (2007). Identifying spatial variability of
26 571 groundwater discharge in a wetland stream using a distributed temperature sensor: *Water Resour.*
27 572 *Research*, v. 43, no. 10, p. W10408. Matheswaran, K., Blemmer, M., Rosbjerg, D., and Boegh, E.
28 573 (2014). Seasonal variations in groundwater upwelling zones in a Danish lowland stream analyzed
29 574 using Distributed Temperature Sensing (DTS). *Hydrol. Process.*, 28, 1422-1435, DOI:
30 575 10.1002/hyp.9690.
31
32
33
34
35 576 McLaughlin, D. L. and M. J. Cohen, (2011), Thermal artifacts in measurements of fine-scale water level
36 577 variation, *Water Resour. Res.*, W09601, doi:10.1029/2010WR010288.
37
38
39 578 McNeill, J. D. (1980). Electromagnetic terrain conductivity measurements at low induction numbers.
40 579 *GEONICS Tech. Note TN6.*, Mississauga, Ont., Canada, Geonics.
41
42
43 580 Rejiba, F., Schamper, C., Chevalier, A., Deleplancque, B., Hovhanissian, G., Thiesson, J., and Weill, P.
44 581 (2018). Multiconfiguration electromagnetic induction survey for paleochannel internal structure
45 582 imaging: a case study in the alluvial plain of the River Seine, France. *Hydrol. Earth Syst. Sci.*, 22,
46 583 159–170, 2018, doi.org/10.5194/hess-22-159-2018.
47
48
49
50 584 Robinson, D. A., A. Binley, N. Crook, F. D. Day-Lewis, T. P. A. Ferré, V. J. S. Grauch, R. Knight, M.
51 585 Knoll, V. Lakshmi, R. Miller, J. Nyquist, L. Pellerin, K. Singha, and L. Slater (2008). Advancing
52 586 process-based watershed hydrological research using near-surface geophysics: a vision for, and
53 587 review of, electrical and magnetic geophysical methods. *Hydrol. Process.*, 22, 3604-3635, 2008,
54 588 DOI: 10.1002/hyp.6963.
55
56
57
58
59
60

- 1
2
3 589 Rosenberry, D.O., Briggs, M.A., Delin, G. and Hare, D.K. (2016). Combined use of thermal methods and
4 590 seepage meters to efficiently locate, quantify, and monitor focused groundwater discharge to a
5 591 sand-bed stream. *Water Resour. Res.*, 52: 4486-4503.
- 6
7
8 592 Rosenberry D.O., and LaBaugh J.W. (2008). Field techniques for estimating water fluxes between surface
9 593 water and ground water. *U.S. Geological Survey Techniques and Methods 4-D2*; 128.
- 10
11
12 594 Sebok, E. and S. Muller (2019), The effect of sediment thermal conductivity on vertical groundwater flux
13 595 estimates, *Hydrol. Earth Syst. Sci.*, 23, 3305–3317.
- 14
15
16 596 Selker, J. S., L. Thevenaz, H. Huwald, A. Mallet, W. Luxemburg, N. van de Giesen, M. Stejskal, J.
17 597 Zeman, M. Westhoff, and M. B. Parlange (2006a). Distributed fiber-optic temperature sensing for
18 598 hydrologic systems. *Water Resour. Res.*, 42, W12202, doi:10.1029/2006WR005326.
- 19
20
21 599 Selker, J., Van de Giesen, N. C., Westhoff, M., Luxemburg, W. M., and Parlange, M. B. (2006b). Fiber
22 600 optics opens window on stream dynamics. *Geophysical Research Letters*, 33, L24401,
23 601 doi:10.1029/2006GL027979.
- 24
25
26
27 602 Sophocleous, M. (2002). Interactions between groundwater and surface water: the state of the science.
28 603 *Hydrogeology Journal*, 52-67, doi.org/10.1007/s10040-001-0170-8.
- 29
30
31 604 Stallman, R. W. (1963). Computation of ground-water velocity from temperature data. *Geological Survey*
32 605 *Water-Supply Paper*, 1544-H, 36-46.
- 33
34
35 606 State Hydraulic Works (2014). *Seyhan Basin Master Plan Report*. State Hydraulic Works, Ankara,
36 607 Turkey.
- 37
38 608 Suzuki, S. (1960). Percolation measurements based on heat flow through soil with special reference to
39 609 paddy fields. *Journal of Geophysical Research*, 65-69.
- 40
41
42 610 Tristram, D.A., Krause, S., Levy, A., Robinson, Z.P., Waller, R.I., and Weatherill, J.J. (2015). Identifying
43 611 spatial and temporal dynamics of proglacial groundwater–surface-water exchange using combined
44 612 temperature-tracing methods. *Freshwater Science*, v. 34, no. 1, p. 99-110.
- 45
46
47 613 Van de Giesen, N., Steele-Dunne, S., Jansen, J., Hoes, O., Hausner, M. B., Tyler, S., and Selker, J. (2012).
48 614 Double-Ended Calibration of Fiber-Optic Raman Spectra Distributed Temperature Sensing Data.
49 615 *Sensors*, 12, 5471-5485; doi:10.3390/s120505471.
- 50
51
52 616 Varli, D., & Yilmaz, K. K. (2018). A Multi-Scale Approach for Improved Characterization of Surface
53 617 Water-Groundwater Interactions: Integrating Thermal Remote Sensing and in-Stream
54 618 Measurements. *Water*, 10, 854; doi:10.3390/w10070854.
- 55
56
57
58
59
60

1
2
3 619 Winter, T. C., Harvey, J. W., Franke, O. L., & Alley, W. M. (1998). Ground Water and Surface Water A
4 620 Single Resource. *U. S. Geological Survey*, Circular 1139.

5
6
7 621

8
9
10 622 **Data Availability Statement**

11
12 623 The data that support the findings of this study are available from the corresponding author upon reasonable
13 624 request.

14
15
16 625

17
18 626

19
20 627

21
22 628

23
24 629

25
26 630

27
28 631

29
30 632

31
32 633

33
34 634

35
36 635

37
38 636

39
40 637

41
42 638

43
44 639

45
46 640

47
48 641

49
50 642

51
52
53
54
55
56
57
58
59
60

Figure Captions:

Figure 1 (a) Regional view of the study basin and location of the reach-scale study area indicated by the red line, (b) Geological formations within the basin (State Hydraulic Works, 2014) and in-stream electrical conductivity (EC; $\mu\text{S}/\text{cm}$) values at the sampling locations (measured on June, 2016)

Figure 2 Piezometer installation units; (a) Metal pointed inner driver rod, (b) Outer metal tube that prevents collapse of the borehole during installation of the piezometer, and (c) driving in installation units into streambed

Figure 3 (a) iButton configurations at each location, (b) photo showing the configuration at location P1 in the June 2018 field trip.

Figure 4 Piper diagram showing ionic composition of samples collected on June, 2016.

Figure 5 EC ($\mu\text{S}/\text{cm}$) results inferred from EMI Survey performed on 31-January-2018. Note that the entire reach shown in this figure is equivalent to the reach indicated in red in Figure 1a, and the stream reach within the rectangle in this figure is the same as the study reach shown in Figure 6.

Figure 6 (a) Map showing the locations of nested piezometers, vertical temperature profiles (iButtons) and DTS transect along with EMI Survey conducted on 27-June-2018 (note that green triangle marker represents an irrigation water diversion barrier). (b) EC data inferred from the EMI survey along the study reach (distance is measured from the downstream end of the transect).

Figure 7 FO-DTS results of two measurement periods: (a,b,c) 18 September, 2018 13:28 -13:53 for which results are effected by shading, (d,e,f) 26 October, 2018 07:31-08:02 with clear temperature anomaly. (a,d) 10-minute air temperature records of the day of measurement from nearest meteorological station; box indicates FO-DTS measurement interval, (b,e) FO-DTS temperature measurement values along the transect (y-axis) in time (x-axis), (c,f) Mean temperature values for each measurement point in time. This graph also shows a moving average of the mean temperature to be able to focus on persistent variations along the transect. Note that the data were deleted from both graphs for sections that FO cable remained out of water. These sections include a barrier location at around 325-328 meters, and another location at 195 meters for the September measurement (b).

Figure 8 (a) air temperature on 26-October-2018, (b) EC data inferred from EMI Survey (June, 2018) overlain by mean top-of-the-streambed temperature values measured by the DTS unit on 26-October- 2018 at time 07:31-08:02, and (c) same as (b) but at time 12:32-13:02. Note that green dashed circles in (c) indicate the effect of sunlight and shading which are not present in (b).

Figure 9 Vertical Hydraulic Gradient (VHG) (%) values calculated using manual water level measurements at (a) site P1, (b) site P2, and (c) site P3 during June-November 2018 period. Note that the VHG values become more positive as going from June, 2018 through November, 2018. Circled VHG values in (b) were deemed suspicious due to clogging of piezometer P2D.

Figure 10 Water level measurements using pressure transducers (HOBO) and vertical hydraulic gradient values at (a) Site P3 and (b) Site P2 during 27-October-2018 to 7-November-2018 period.

Figure 11 (a) Air temperature, (b) raw temperature data series, (c) amplitude variation and (d) estimated vertical flux values at site P3 for the 26-October-2018 to 7-November-2018 measurement period.

Table 1. FO-DTS measurement time periods and statistics together with air temperature and stream discharge at nearest meteorological station and Çakıt stream gauging station, respectively.

FO-DTS Measurements		FO-DTS Stream Measurement (°C)			Air Temperature (°C)			Stream Discharge (m ³ /s)
Date	Time	Min	Mean	Max	Min	Mean	Max	
27-June-2018	17:51-18:14	19.51	19.96	20.45	29.82	29.93	30.12	0.754
28-Jun- 2018	11:18-12:12	16.51	17.69	18.80	28.52	29.25	29.72	0.711
	17:49-18:31	19.22	19.86	20.45	25.22	25.86	26.51	
18-Sep-2018	10:49-11:15	14.37	15.10	16.03	21.91	22.09	22.18	0.817
	13:28-13:53	16.90	17.56	18.22	24.48	24.60	24.83	
	17:33-17:48	15.76	16.53	17.24	23.58	23.88	24.14	
25-Oct- 2018	07:41-08:11	11.17	11.66	12.17	10.58	11.59	12.42	0.672
	10:54-11:34	11.34	11.87	12.39	10.51	10.59	10.76	
	12:15-12:45	11.90	12.44	12.97	11.49	11.55	11.68	
	14:48-15:18	12.19	12.68	13.22	7.81	9.19	11.43	
26-Oct-2018	07:31-08:02	8.88	9.53	10.09	2.62	3.24	3.58	0.678
	10:51-11:21	9.18	9.69	10.21	2.15	2.50	2.83	
	12:32-13:02	9.73	10.43	11.11	4.59	5.22	5.51	

1
2
3
4
5
6
7
8
9
10
11
12
13
14
15
16
17
18
19
20
21
22
23
24
25
26
27
28
29
30
31
32
33
34
35
36
37
38
39
40
41
42
43
44
45
46
47
48
49
50
51
52
53
54
55
56
57
58
59
60

Table 2. Vertical flux estimates using VFLUX

Time Period	Site	Depth below top of streambed (cm)	Vertical flux (m/s)	Flow direction
28.06.2018 - 02.07.2018	P1	9.5	(+2.2x10 ⁻⁶) - (+2.5x10 ⁻⁶)	Downward
18.09.2018 - 03.10.2018	P2	9.5	(-5x10 ⁻⁷) - (-2x10 ⁻⁶)	Upward
	P3	5.5	(-1x10 ⁻⁶) - (-1x10 ⁻⁵)	Upward
26.10.2018 - 07.11.2018	P2	9.5	(+6x10 ⁻⁷) - (+1x10 ⁻⁶)	Downward
	P3	9.5	(-2x10 ⁻⁶) - (-3x10 ⁻⁶)	Upward

For Peer Review

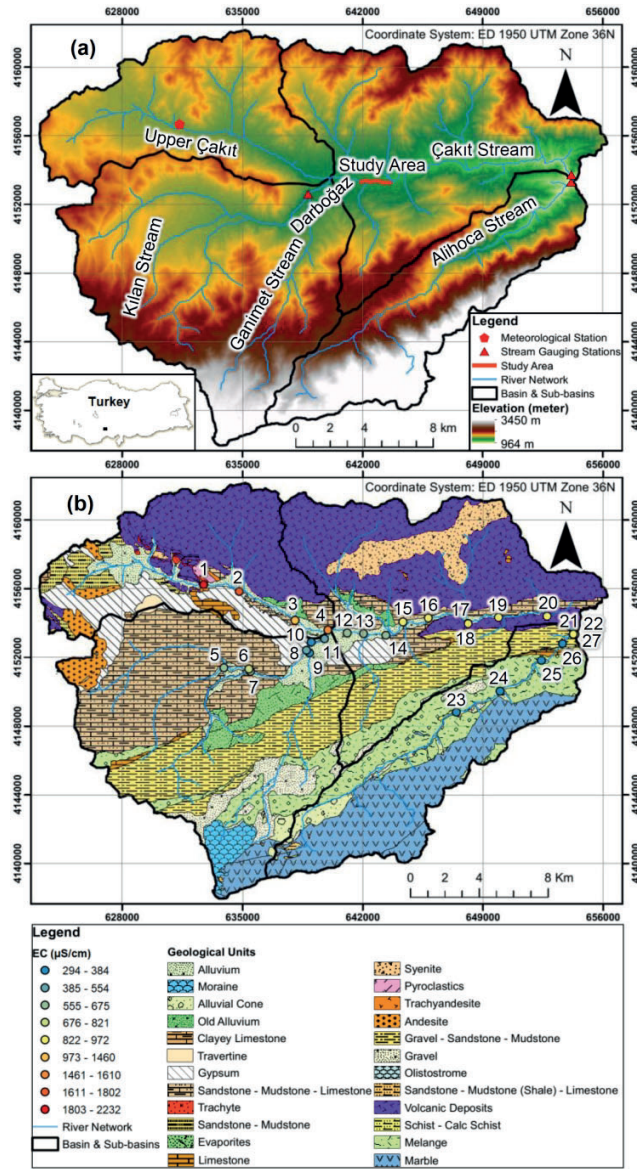


Figure 1 (a) Regional view of the study basin and location of the reach-scale study area indicated by the red line, (b) Geological formations within the basin (State Hydraulic Works, 2014) and in-stream electrical conductivity (EC; $\mu\text{S}/\text{cm}$) values at the sampling locations (measured on June, 2016)

1
2
3
4
5
6
7
8
9
10
11
12
13
14
15
16
17
18
19
20
21
22
23
24
25
26
27
28
29
30
31
32
33
34
35
36
37
38
39
40
41
42
43
44
45
46
47
48
49
50
51
52
53
54
55
56
57
58
59
60

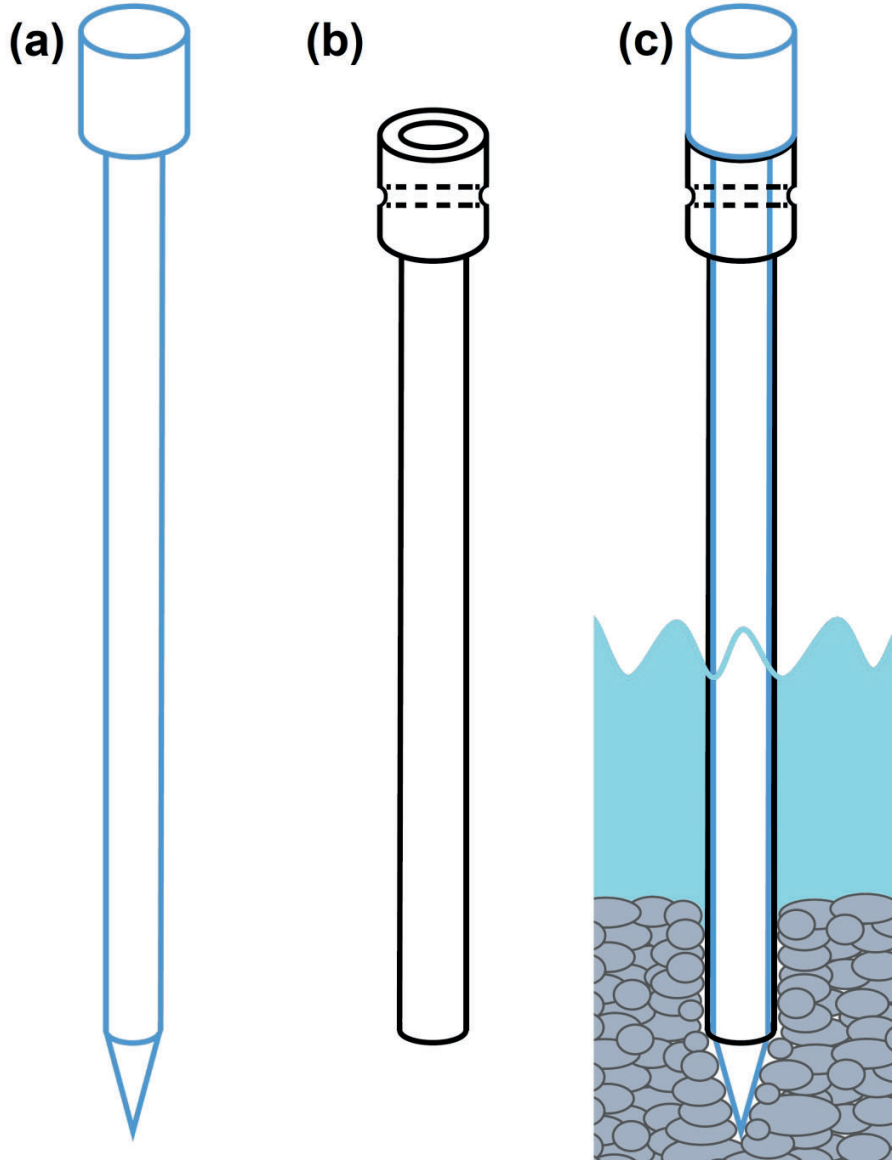


Figure 2 Piezometer installation units; (a) Metal pointed inner driver rod, (b) Outer metal tube that prevents collapse of the borehole during installation of the piezometer, and (c) driving in installation units into the streambed

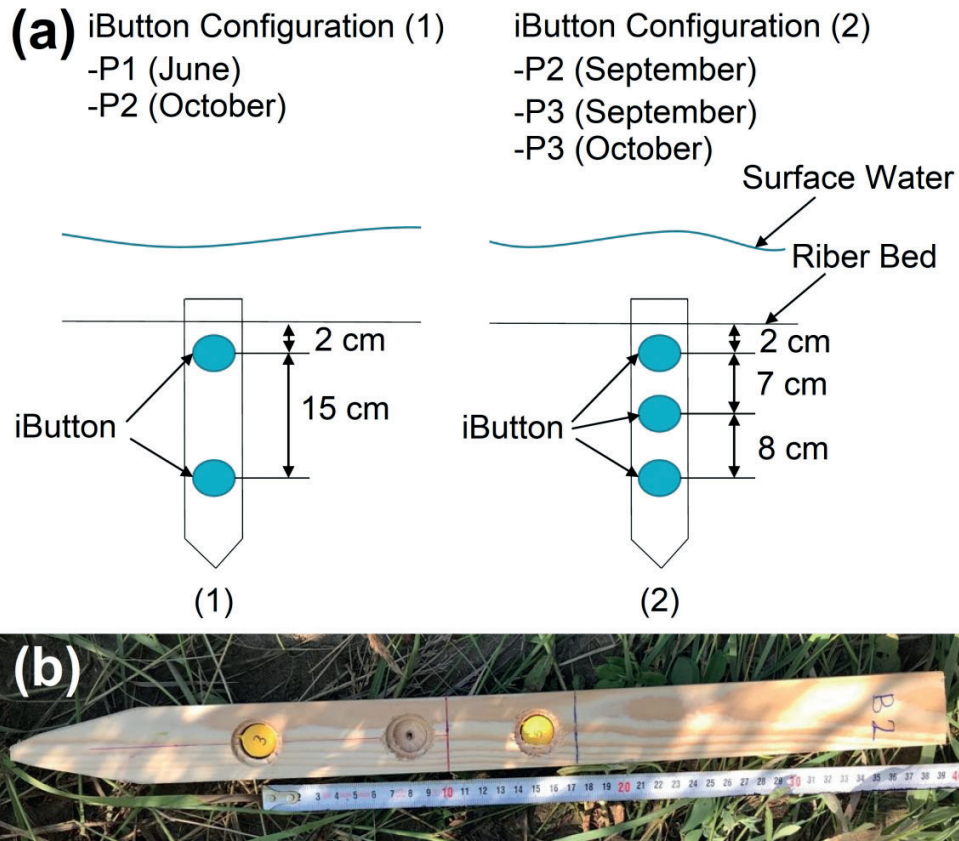


Figure 3 (a) iButton configurations at each location, (b) photo showing the configuration at location P1 in the June 2018 field trip.

1
2
3
4
5
6
7
8
9
10
11
12
13
14
15
16
17
18
19
20
21
22
23
24
25
26
27
28
29
30
31
32
33
34
35
36
37
38
39
40
41
42
43
44
45
46
47
48
49
50
51
52
53
54
55
56
57
58
59
60

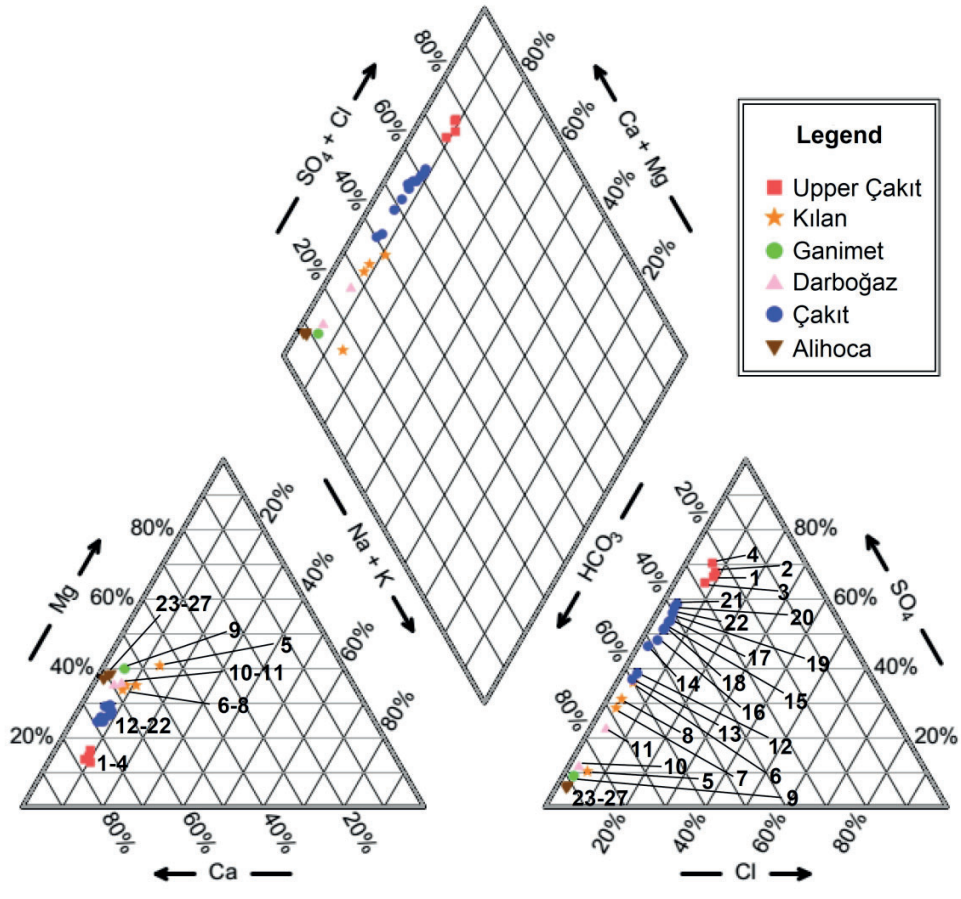


Figure 4 Piper diagram showing ionic composition of samples collected on June, 2016.

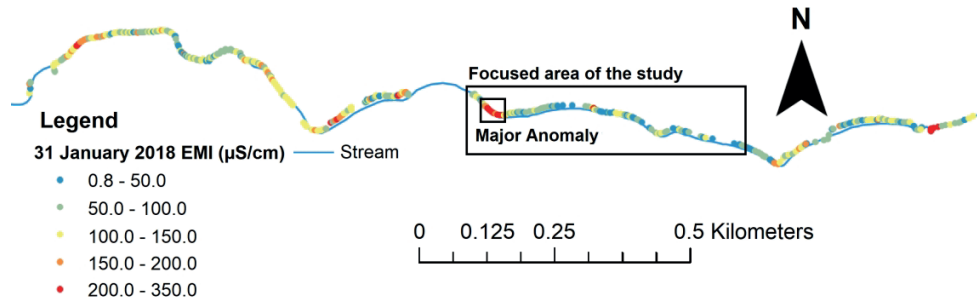


Figure 5 EC ($\mu\text{S}/\text{cm}$) results inferred from EMI Survey performed on 31-January-2018. Note that the entire reach shown in this figure is equivalent to the reach indicated in red in Figure 1a, and the stream reach within the rectangle in this figure is the same as the study reach shown in Figure 6.

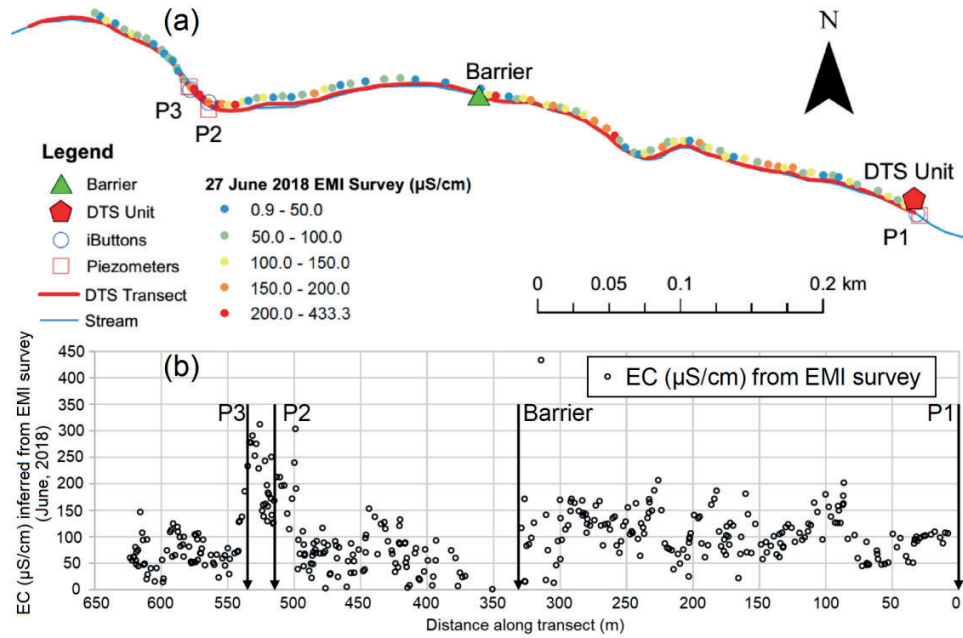


Figure 6 (a) Map showing the locations of nested piezometers, vertical temperature profiles (iButtons) and DTS transect along with EMI Survey conducted on 27-June-2018 (note that green triangle marker represents an irrigation water diversion barrier). (b) EC data inferred from the EMI survey along the study reach (distance is measured from the downstream end of the transect).

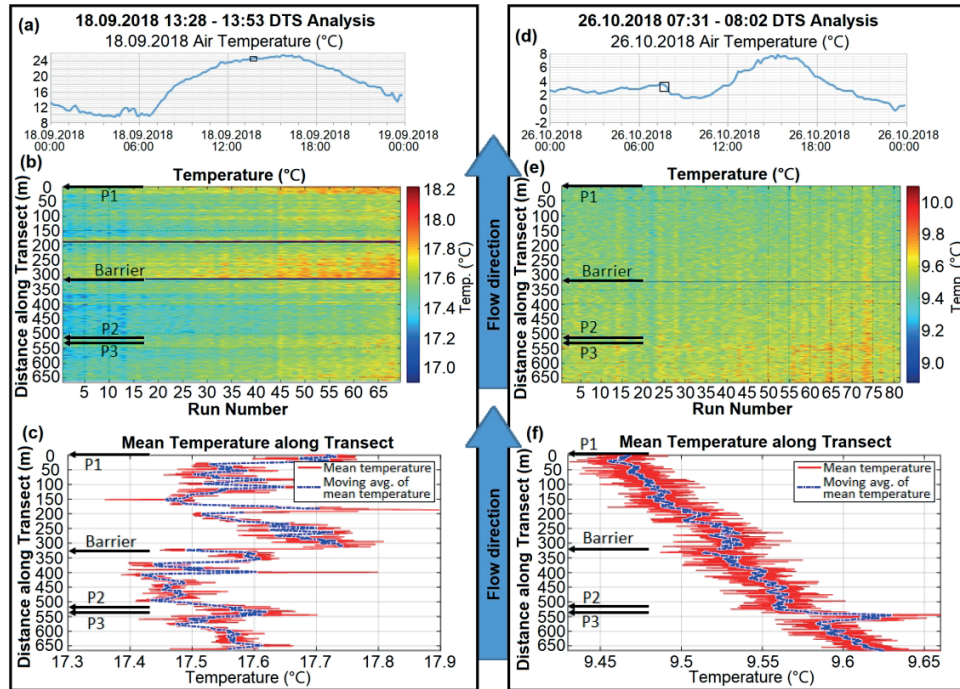


Figure 7 FO-DTS results of two measurement periods: (a,b,c) 18 September, 2018 13:28 -13:53 for which results are affected by shading, (d,e,f) 26 October, 2018 07:31-08:02 with clear temperature anomaly. (a,d) 10-minute air temperature records of the day of measurement from nearest meteorological station; box indicates FO-DTS measurement interval, (b,e) FO-DTS temperature measurement values along the transect (y-axis) in time (x-axis), (c,f) Mean temperature values for each measurement point in time. This graph also shows a moving average of the mean temperature to be able to focus on persistent variations along the transect. Note that the data were deleted from both graphs for sections that FO cable remained out of water. These sections include a barrier location at around 325-328 meters, and another location at 195 meters for the September measurement (b).

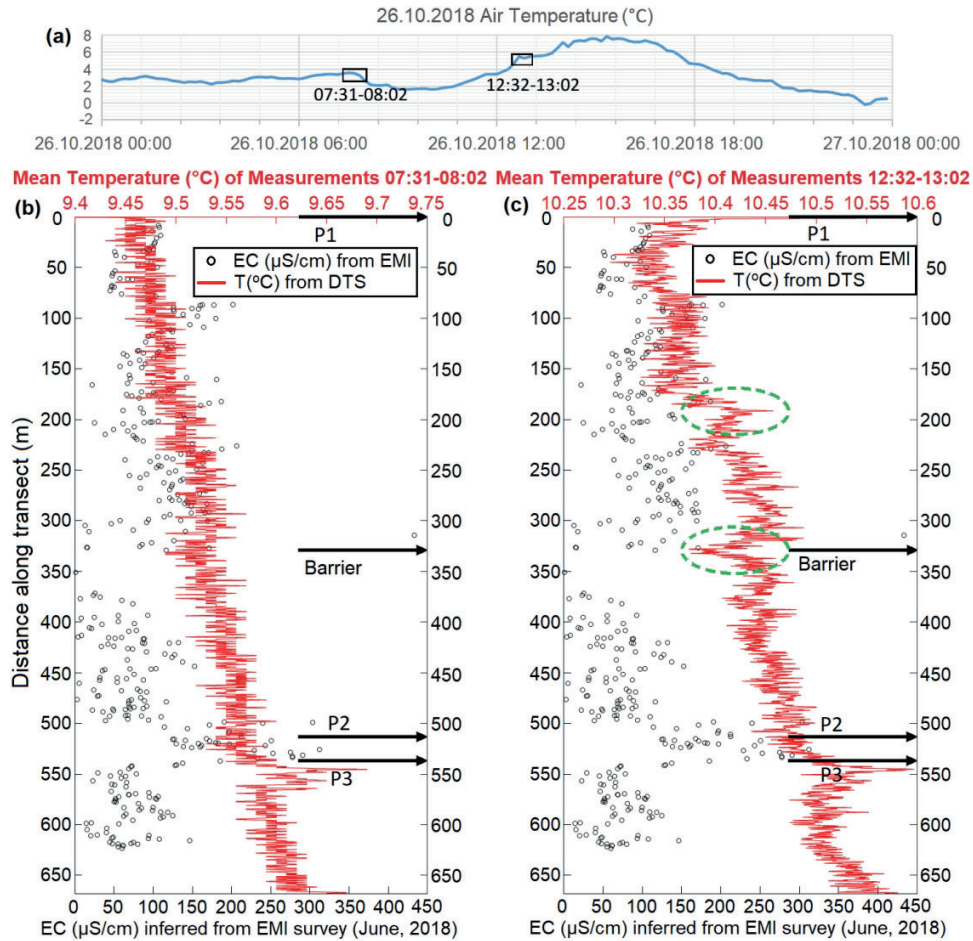


Figure 8 (a) air temperature on 26-October-2018, (b) EC data inferred from EMI Survey (June, 2018) overlain by mean top-of-the-streambed temperature values measured by the DTS unit on 26-October- 2018 at time 07:31-08:02, and (c) same as (b) but at time 12:32-13:02. Note that green dashed circles in (c) indicate the effect of sunlight and shading which are not present in (b).

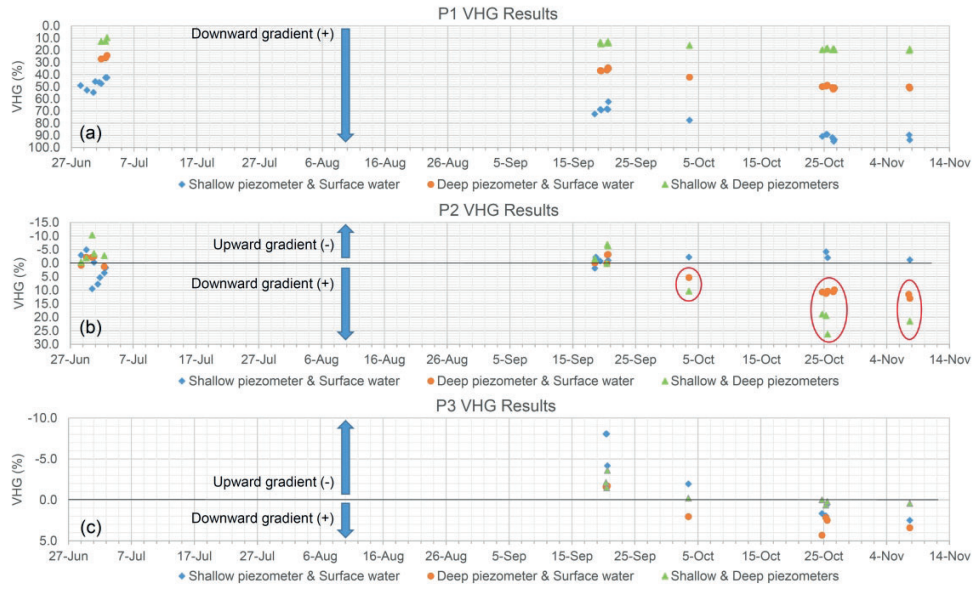


Figure 9 Vertical Hydraulic Gradient (VHG) (%) values calculated using manual water level measurements at (a) site P1, (b) site P2, and (c) site P3 during June-November 2018 period. Note that the VHG values become more positive as going from June, 2018 through November, 2018. Circled VHG values in (b) were deemed suspicious due to clogging of piezometer P2D.

1336x812mm (96 x 96 DPI)

1
2
3
4
5
6
7
8
9
10
11
12
13
14
15
16
17
18
19
20
21
22
23
24
25
26
27
28
29
30
31
32
33
34
35
36
37
38
39
40
41
42
43
44
45
46
47
48
49
50
51
52
53
54
55
56
57
58
59
60

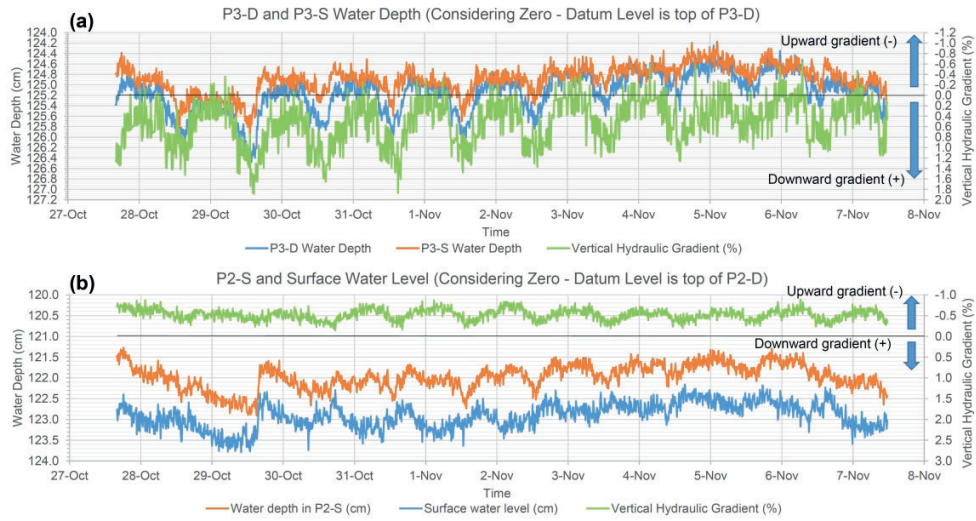


Figure 10 Water level measurements using pressure transducers (HOBO) and vertical hydraulic gradient values at (a) Site P3 and (b) Site P2 during 27-October-2018 to 7-November-2018 period.

1116x597mm (120 x 120 DPI)

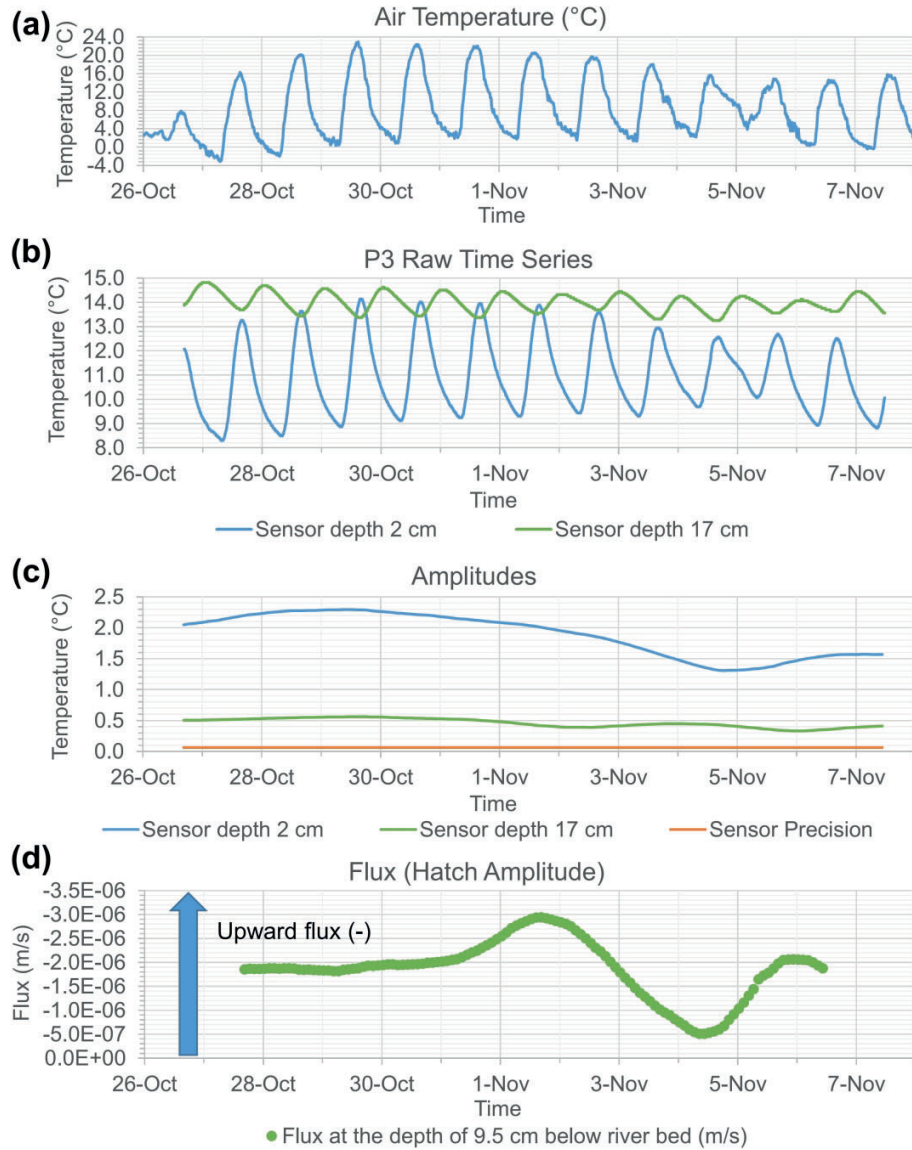
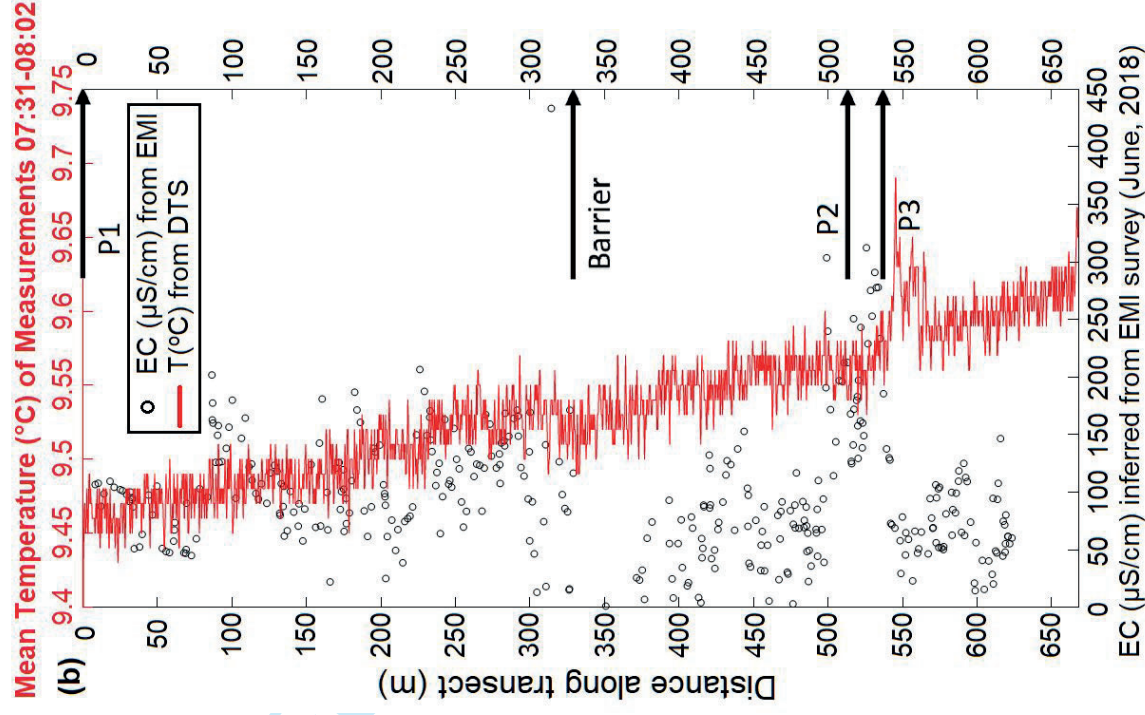


Figure 11 (a) Air temperature, (b) raw temperature data series, (c) amplitude variation and (d) estimated vertical flux values at site P3 for the 26-October-2018 to 7-November-2018 measurement period.

831x1048mm (96 x 96 DPI)

- 1
2
3
4
5
6
7 ● Geophysical techniques and in-stream
8 measurements were coupled in a hierarchical
9 manner.
10
11 ● The Electromagnetic Induction (EMI) surveys served
12 as a reconnaissance method at long stream reaches
13 to identify preferential groundwater-stream
14 exchange locations
15 ● Distributed Temperature Sensing (DTS) method was
16 further utilized as a complementary method over
17 shorter distances to provide continuous
18 observations in time and space in support of EMI
19 surveys.
20 ● Anomalies from EMI and DTS measurements
21 coincided.
22 ● Once anomaly locations were obtained point-based
23 methods (piezometers and thermochrons) provided
24 quantitative results.



A multi-technique approach to determine temporal and spatial variability of groundwater-stream water exchange

Kasimcan Koruk, Koray Kamil
Yilmaz*, Zuhail Akyurek, Andrew
Binley